IRANIAN JOURNAL OF CATALYSIS

Preparation and characterization of SnO_2-$BiVO_4$-CuO catalyst and kinetics of phenazopyridine photodegradation

Ailin Yousefi, Alireza Nezamzadeh-Ejhieh*

Department of Chemistry, Shahreza Branch, Islamic Azad University, P.O. Box 311-86145, Shahreza, Isfahan, Iran.

Received 11 March 2021; received in revised form 11 May 2021; accepted 12 May 2021

ABSTRACT

Here, SnO_2, $BiVO_4$, and CuO nanoparticles (NPs) were hydrothermally synthesized and mixed in an agate mortar mechanically. The coupled ternary SnO_2-$BiVO_4$-CuO (SBC) catalyst and the individual NPs were then briefly characterized by powder X-ray diffraction (XRD), scanning electron microscope (SEM), and diffuse reflectance spectroscopy (DRS). Average crystallite size of 25 nm was obtained from the XRD data based on the Scherrer formula. The absorption edge (λ_{AE}) values of 1095, 430, 558, and 636 nm, corresponding to the band gap (Eg) values of 1.13, 2.88, 2.22, and 1.95 eV, were respectively obtained for the as-synthesized CuO, SnO_2, and $BiVO_4$ NPs and the as-prepared ternary SBC catalyst based on DRS results. The PZP degradation% of 11, 15, 17, and 24% were obtained by the CuO, SnO_2, $BiVO_4$ NPs, and SBC catalyst (with the same moles of each component). But, when the moles of $BiVO_4$ in the SBC were two times greater than the others, about 43% of PZP were removed. The k-value of 9.9×10^{-3} min^{-1} corresponding to the $t_{1/2}$-value of 70 min was obtained by applying the Hinshelwood plot on the photodegradation results. Photodegradation experiments were carried out in pH 5, C_{PhP}: 3.35 ppm, and catalyst dosage: 0.55 g L^{-1}. Further, when the photodegraded solutions were subject to the COD experiment, the Hinshelwood plots showed a slope of 0.01 min^{-1} which corresponds to the $t_{1/2}$-value of 69.3 min.

***Keywords**: Photodegradation, SnO_2-$BiVO_4$-CuO heterogeneous catalyst, Phenazopyridine.*

1. Introduction

Nowadays, our environment is critically polluted by various hazards such as heavy metals, pharmaceutics, organic and inorganic compounds. These chemicals are introduced into the environment by the discharge of industrial, hospital, and domestic sewage into the environment. Unfortunately, due to the population growth in recent decades, an increased need in people's lives for novel technologies and products is causing the discharging of higher amounts of waste water into the environment. In contrast, this increased world population must benefit of the human essential needs including safe drinking water. Thus, before discharging such effluents into the environment, their toxicity has to be decreased to the allowed levels. For this goal, introducing novel technologies or developing/enhancing traditional removal technologies is very important for analytical/environmental chemists [1-10].

*Corresponding author:
E-mail address: *arnezamzadeh@iaush.ac.ir* (**A. Nezamzadeh-Ejhieh**)

Further, introducing effective technologies such as electrochemical sensors for sensing and quantifying low levels of various pollutants has become of high interest [11-13].

Semiconducting-based photocatalysis is an efficient technology that has been widely used for the degradation/mineralization of organic/inorganic compounds and even for the reduction of some hazardous heavy metals. In this heterogeneous process, when a semiconducting material is irradiated by suitable photons with an energy photon equal to or greater than the energy gap (Eg) of the semiconductor, commonly in the UV and visible regions of the light, the electron and hole (e^-/h^+) pairs can be induced in the conduction band (CB) and valence band (VB) of the semiconductor, respectively. The e^-/h^+ pairs can, directly and indirectly, participate in the degradation of the subjected pollutant. The photoinduced electrons are the potent reducing agents that can begin the degradation of the pollutant via the reduction process. In contrast, the photoinduced holes are the potent oxidizing agents that can directly

attack the organic pollutants and oxidize them to begin the degradation process. In an indirect way, the photoinduced electrons can reduce the dissolved oxygen to yield the powerful reactive superoxide radicals. In contrast, the photoinduced holes can attack the water molecules or hydroxyl anions to yield hydroxyl radicals as powerful oxidizing agents. These powerful reactive radicals can effectively attack the organic molecules and degrade them into smaller intermediates. Further attacks to these intermediates mineralize them into water, carbon dioxide, and other inorganic species. Overall, in semiconducting-based photocatalysis, four main reactive species of the photogenerated electrons and holes, superoxide and hydroxyl radicals are responsible for degrading the molecules of the pollutants into harmless intermediates, water, carbon dioxide, etc. [14-22].

Unfortunately, the photogenerated e^-/h^+ pairs may recombine and drastically reduce the overall efficiency of a typical photodegradation process. The overall effects of all the processes mentioned above depend on the extent of e^-/h^+ production. Thus, various strategies have been used to decrease the extent of e^-/h^+ recombination. In the nano-sized strategy, a drastic decrease occurs in the path length in which the photoinduced e^-/h^+ pairs should travel from the bulk of the semiconductor to the surface. This causes faster traveling of the e^-/h^+ pairs to the surface. Thus, they can participate in the photodegradation process before they recombine again [23-26]. Another strategy is doping of metals/non-metals into the semiconductor, which creates some novel/mixed energy levels in the systems. Thus, the photogenerated e^-/h^+ pairs in the CB/VB of the primary semiconductor can immigrate to these novel energy levels, and the e^-/h^+ recombination tends to decrease [27-29]. In a supporting way, suitable support such as alumina, silica, zeolite, etc. can be used for dispersing of the semiconductor species on their surface. This prevents the aggregation of semiconductor species and increases the effective surface area [30, 31]. Further, the zeolitic supports have a permanent internal electric field that effectively interacts with the photoinduced e^-/h^+ pairs and disperses them through the zeolite network [32, 33].

Another strategy for decreasing the e^-/h^+ recombination is the coupling of two or more semiconductors with the suitable potential positions of CB and VB (hybriding, or hetero-junction systems). In such systems, the internal redox (reduction-oxidation) processes occur between the CB levels of the semiconductors and the VB levels. These redox processes drastically prevent the e^-/h^+ recombination [34-39]. In this regard, the various mechanisms, including direct Z-scheme, type II-Heterojunction, etc have been illustrated and reviewed for the photodegradation processes [40-46]. The plasmonic systems are another strategy for enhancing the separation of the charge carriers in the photoexcited semiconductors. A plasmon is considered a quasiparticle, and in the visible region of light, the coupling of photons creates another quasiparticle called a plasmon polariton. Some metal nanoparticles, such as Au, Ag, Cu, etc, have the surface plasmon resonance (SPR) effect. SPR is considered a collection of oscillations of the electrons in the conduction band of metal NPs under electromagnetic field irradiation. This effect can convert visible light to chemical energy and separates the photoinduced e^-/h^+ pairs produced on the surface of the semiconductor. Generally, the plasmonic sensitizers enhance the absorption of visible light photons without the problem of degradation encountered by organic sensitizers [47-50].

Based on the discussion mentioned above, we aimed to construct a ternary catalytic system with the visible light activity of its components. Another aspect was the selection of a system with rarely using concerning other systems. Further, the VB and CB levels' potential position is suitable for an efficient charge transfer process because the charge carrier transfer between the photoexcited semiconductors occurs via the internal redox processes in the coupled system. Thus, $BiVO_4$, CuO, and SnO_2 NPs were selected for coupling. The resulting ternary SnO_2-$BiVO_4$-CuO (SBC) coupled system and individual systems were briefly characterized by XRD, SEM-EDX, FTIR, etc. The ternary coupled system showed a boosted photocatalytic activity compared to the individual systems in the photodegradation of phenazopyridine (PZP). The work then focused on the kinetics of the process. COD estimated the relative mineralization of PZP. The rate of photodegradation and photo mineralization of PZP was also compared.

2. Experimental

2.1. Materials and synthesize procedures

Chemicals used were $Bi(NO_3)_3.5H_2O$ (99.9%), NH_4VO_3 (99.9%), $SnCl_2.2H_2O$ (99.9%), $Cu(NO_3)_2.3H_2O$ (99.9%), Na_2CO_3 (99.9%), etc, as analytical reagents, were sourced from Merck or Aldrich Co. A 100 mg phenazopyridine tablet (chemical formula: $C_{11}H_{11}N_5$. MW: 213.24) was purchased from Shahrdaro Co., Iran.

For preparing phenazopyridine (PZP) solution, the following procedure was followed. One tablet was weighed, at 175 mg. Then, five tablets were added to an agate mortar and powdered. Then, aliquot 1.75 mg of the powder was transferred into a 100 mL volumetric

flask. After dilution, it reached the mark by water. The prepared solution is considered a 10 mg/L PZP solution.

For preparing CuO nanoparticles (NPs), a precipitation method was used in which 3000 mg copper nitrate tree hydrate was weighed, dissolved in water and diluted in a 50 mL volumetric flask. The solution pH was adjusted by 1 M sodium carbonate solution at 10. The solution was aged for 12 h in ambient conditions. Solid sediment resulted was separated by filtration and washed with water then dried at 60 °C for 24 h and then calcined at 350 °C for 4 h [51].

The following procedure was used to synthesize SnO_2 NPs. 50 mL 0.1 M Sn(II) solution (from $SnCl_2.2H_2O$) was prepared and added to a 100 mL beaker. Then, about 4 mL ammonia solution was added, and the resulting mixture was magnetically stirred for 20 min. The resulting white precipitate was aged in the mother liquor for 12 h. After centrifugation at >13000 rpm, the solid material was thoroughly washed with hot water. After drying at room temperature, it was calcined at 600 °C for 24 h. Then, it was powdered thoroughly and heated again at 600 °C for another 4 h [52].

Finally, the following procedure was used to synthesize $BiVO_4$ NPs. 20 mmole $Bi(NO_3)_3.5H_2O$ was added to 20 mL nitric acid (65%) and wholly dissolved (solution A). A 20 mmole NH_4VO_3 was added in 20 mL 0.1 M NaOH solution and completely dissolved (solution B). After adding solution A to B, it was magnetically stirred for 2 h at room temperature. The pH of the stable homogeneous suspension was adjusted at 7 by 0.1 M NaOH. Then, the suspension was transferred into a Teflon-lined stainless autoclave. The reactor was then heated at 180 °C for 6 h. The hydrothermally synthesized product was then separated by centrifugation (>13000 rpm, g: 15493). The yellow product was washed with copious water and dried at 80 °C for 12 h. The resulting $BiVO_4$ NPs were stored in the dark for the next steps [53].

Finally, to prepare the ternary SnO_2-$BiVO_4$-CuO samples with different SnO_2:$BiVO_4$:CuO mole ratios, the required amount of each component was weighed and thoroughly hand mixed in an agate mortar for 15 min. Homogenous powders were obtained that were used in the photodegradation experiments.

2.2. Characterization

The following techniques/instruments were used to characterize the as-prepared samples for carrying out this work.

SEM (TESCAN CO., Czech Republic), XRD (X'Pertpro, with Ni-filtered and Cu-Kα radiation at 1.5406 Å, V: 40 kV, i: 30 mA; Netherland), UV-Vis spectrophotometer equipped with an optics integrating sphere and a diffuse reflectance accessory (JASCOV670, using $BasO_4$ as reference, A pH meter (Jenway model 3505), A centrifuge instrument (Sigma, 2-16P, Germany), A photoluminescence spectrophotometer (Perkin ELmer S45, U.K.).

2.3. Photodegradation experiments

In a typical run, 10 mL suspension of 5.5 mg/L of the SnO_2-$BiVO_4$-CuO (SBC) system and 3.4 mg/L PZP was added into a 20 mL beaker, and the pH was adjusted at 5. The suspension was then shaken in the dark for 15 min and then irradiated by a moderate pressure Hg-lamp (35 W, Philips, type G-line with maximum emission at 435.8 nm, positioned 15 cm above the cell) under magnetic stirring (at 200 rpm). The sampling was made at definite times, and the withdrawn suspension was centrifuged (>13000 rpm). The absorption spectrum of the supernatant was then recorded on a UV-Vis spectrphotometer. The absorbance at λ_{max} 430 nm was recorded (A) and compared with that of blank PZP solution (without the catalyst). The C/Co value was calculated as a measure of PZP removal. The following **Eq. 1** was used for the PZP photodegradation extent.

$$D\% = [(1-A/A_o)] \times 100 \quad \textbf{(1)}$$

3. Result and Discussion

3.1. Characterizations

3.1.1. XRD Patterns

To study the crystalline structure of the as-prepared SnO_2-$BiVO_4$-CuO (SBC) system, the X-ray diffraction technique was used as a powerful technique for this goal [54, 55]. The typical diffraction pattern for the SBC sample is shown in **Fig. 1**, which includes the corresponding diffraction peaks of the constituent components. Thus, the peaks were assigned to the corresponding *hkl* planes based on the following illustration.

The corresponding peaks of the SnO_2 component agreed with the rutile SnO_2 crystalline structure based on the diffraction peaks positioned at 2-tetha values of 26.6° (110), 33.9° (101), 38.0° (200), 51.8° (211), 57.9° (002), 62.0° (310), 66.0° (301), 71.3° (202), and 78.7° (321) [38,39]. Further, a monoclinic $BiVO_4$ crystalline phase was detected in the pattern because some peaks agreed with the diffraction peaks of 18.66º (101), 28.85º (200), 30.5º (211), 32.72º (112), 34.5º (220), 39.78º (301), 40.4º (103), 46.71º (321), 50.28º (213), 53.22º (411), 58.3º (004), and 59.43° (332). This agreement is based on the JCPDS no: 00-014-0688 [58, 59].

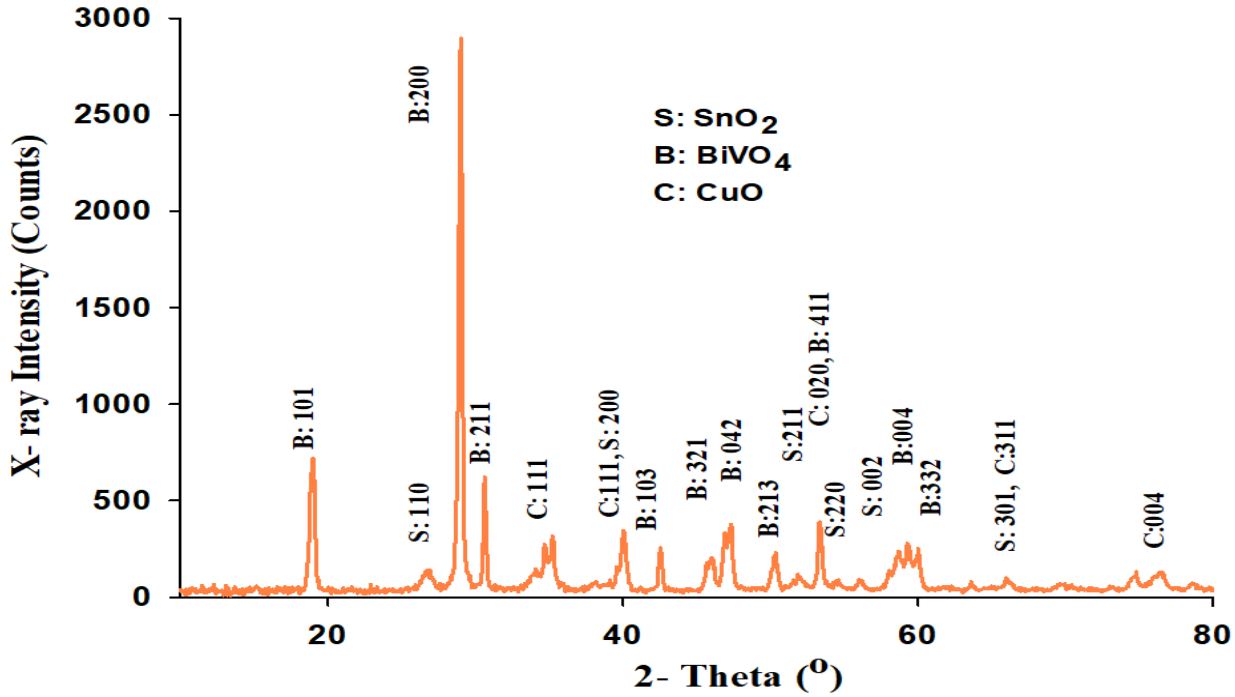

Fig. 1. XRD patterns of the ternary SnO_2-$BiVO_4$-CuO coupled system with a SnO_2:$BiVO_4$: CuO mole ratio of 1:2:1.

Finally, the presence of the monoclinic CuO crystals was detected for the CuO component in the ternary catalyst because some diffraction peaks agreed with this crystalline phase based on the JCPDS card no. 48-1548. According to this standard pattern, the monoclinic phase of CuO has typical diffraction peaks at 2-theta positions of 32.47° (110), 35.49° (-111), 38.68° (111), 48.65° (202), 53.36° (020), 58.25° (220), and 61.45° (022). For this crystallite phase, the most intense diffraction peaks are located at 2θ positions of 35.49° and 38.68°, commonly used to identify the CuO monoclinic phase [60-62].

In X-ray diffraction and crystallography, the size of sub-micrometer crystallites in a solid can be related to the broadening of a diffraction peak by the Scherrer equation. **Eq. 2** is shown below, and it is commonly used for estimating the size of crystals in powder form.

$$d = (k\lambda)/(\beta\cos\theta) \qquad \textbf{(2)}$$

is the mean size of the ordered (crystalline) domains (the crystallite size). This size may be smaller or equal to the grain size, which may be smaller or equal to the particle size. Dimensionless shape factor (k), commonly has a value of about 0.9 and varies with the actual shape of the crystallite. 'λ' is the X-ray wavelength, and β is the line broadening at half the maximum " FWHM: in radians). The reported value for βsubtractinginstrumental line broadening from the total value. Finally, θ is the Bragg angle. When the angle between the incident wave vector and the scattered wave vector has considered in the corrections, which is different from the θ in the 2θ scan, k is about 0.88, and this equation has called the Scherrer equation with k=0.88. This only applies to a perfect 1D set of planes. In an experimentally 3D case, the crystal lattice type and the size and shape of the nanocrystallite affect the structure factor or scattering function S(q), and hence the peaks. Thus a correction for FWHM should be done. For example, for a spherical crystallite with a cubic lattice, the diameter of a spherical nanocrystal can be related to the peak FWHM by applying k=1.11.

This equation is not usable for grains larger than about 0.1 to 0.2 μm. Its use is limited to nano-scale crystallites and, even more stringently, the coherently scattering domain size smaller than the crystallite size (due to factors mentioned below). Generally, various factors include the inhomogeneous strain and crystal lattice imperfections (the most critical factor), instrumental effects, dislocations, sub-boundaries, stacking faults, grain boundaries, twinning, micro stresses, coherency strain, chemical heterogeneities, and crystallite smallness affect the width of a diffraction peak. These factors result in the peak shift, peak broadening and asymmetry, anisotropic or other peak shape effects. Thus, the Scherrer equation gives a lower bound on the coherently scattering domain size or the crystallite size. In the zero effects of all factors, the peak width depends on the crystallite size and the Scherrer formula can be applied. The Scherrer formula can predict an extra peak width coming from the other factors and a larger

crystallite size. It is worth mentioning that the Scherrer equation gives us the crystallite size, not particle size. Particle is often agglomerations of many crystallites, and thus, the crystallite size can be considered a lower limit of particle size. Thus, XRD gives no information about the particle size. For direct measuring particle size, some techniques such as visible light scattering, image analysis, and sieving can be used [63-68].

Thus, the data obtained from the XRD pattern of the SBC sample was used to calculate the crystallite size. All data are summarized in **Table 1**. Average crystallite size of about 25 ± 8 nm was obtained for the catalyst.

3.1.2. UV-Vis absorption spectra of the catalysts

Fig. 2 shows typical UV-Vis absorption spectra for the single SnO_2, $BiVO_4$, and CuO powder catalysts and the ternary SnO_2-$BiVO_4$-CuO system. The absorption future is a result of the electronic transition during the photoexcitation of the samples. Thus, the consumed energy can be used to estimate the band gap energy for the sample [69]. Based on the spectra, CuO showed a broad absorption peak covering the whole range of UV-Vis and near-IR regions of light. Thus, the as-synthesized CuO can absorb the photons in the regions mentioned above. When these semiconductors were coupled, the overall absorption peak was red-shifted concerning the SnO_2 alone. This proves that this ternary catalyst drastically enhanced the optical properties of SnO_2 NPs.

Absorption edge (λ_{AE}) values for the samples were estimated by the extrapolation of the downward slopes of the curves. The crossing point with the x-axis gives the value of the λ_{AE}. The λ_{AE}-values of 1095, 430, 558, and 636 nm were obtained for the as-synthesized CuO, SnO_2, and $BiVO_4$ NPs, and the as-prepared ternary catalyst, respectively. The values were then substituted in the following **Eq. 3** to estimate the band gap energy (Eg) for the samples [70-72].

$$E_g\ (eV) = 1240 / \lambda_{AE}\ (nm) \qquad \textbf{(3)}$$

Eg-values of 1.13, 2.88, 2.22, and 1.95 eV were obtained for CuO, SnO_2, and $BiVO_4$ NPs and the as-prepared ternary catalyst, respectively.

Table 1. Results used in the Scherrer in the estimation of the crystallite size of SnO_2-$BiVO_4$-CuO ternary catalyst.

2θ	FWHM (2θ)	β	cosθ	β cosθ	d (nm)	Av. d (nm)
18.97	0.3936	0.0068	1	0.0068	20.38	
46.02	0.2952	0.0051	1	0.0051	27.17	
46.94	0.1968	0.0034	1	0.0034	40.76	25 ± 8
51.98	0.492	0.0085	1	0.0085	16.30	
76.47	38.23	0.0068	1	0.0068	20.38	

3.1.3. SEM results

To elucidate the morphology of the as-prepared ternary SnO_2-$BiVO_4$-CuO system, it was characterized by a scanning electron microscope as a helpful tool for this goal [73-75]. Two SEM images are shown in **Fig. 3**. The pictures were subject to the image-j software for estimating the particle size distribution. As shown in the insets, most particles have a nano-dimension. Overall, the particles have a semi-spherical morphology. By focusing on the images, some plate-like species are present in some places related to SnO_2 species.

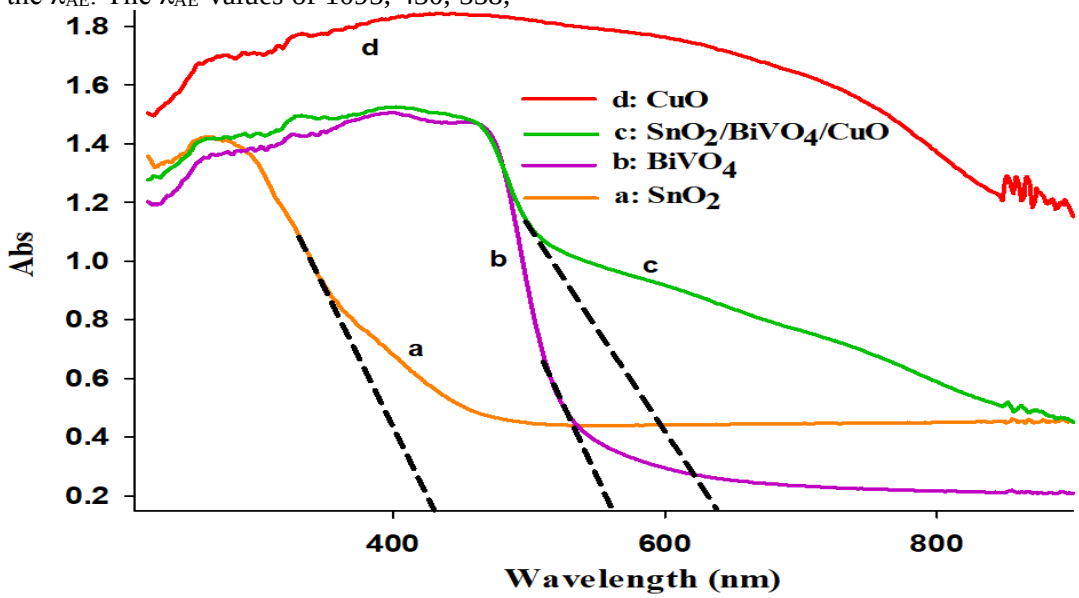

Fig. 2. Typical UV–Vis absorption DRS spectra and SnO_2, $BiVO_4$, and CuO and the resulting ternary SnO_2-$BiVO_4$-CuO coupled system with a SnO_2:$BiVO_4$:CuO mole ratio of 1:2:1.

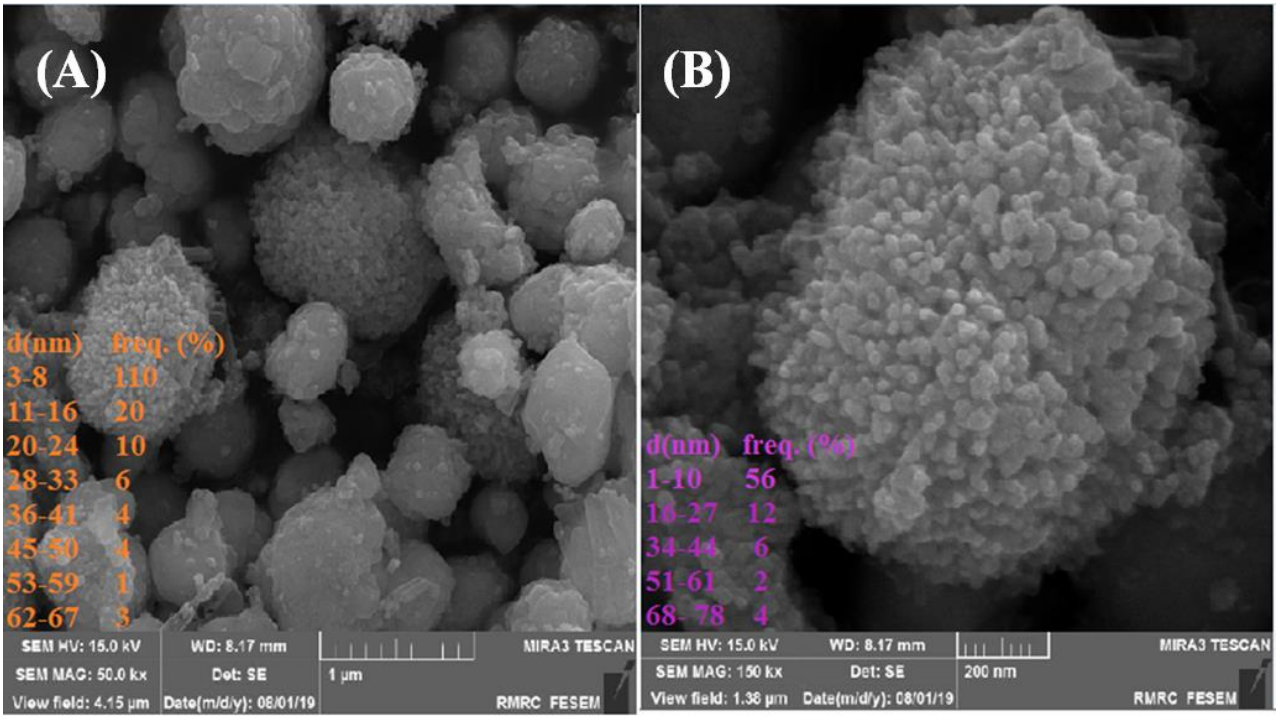

Fig. 3. A, B) SEM images of ternary SnO_2-$BiVO_4$-CuO coupled system (SnO_2:BiV_4:CuO mole ratio of 1:2:1).

3.2. Photodegradation results

3.2.1. Photocatalytic activity

In the initial steps of the work, the effects of the surface adsorption and direct photolysis were investigated in the PZP removal. Further, the effects of the heterogeneous photocatalysis by the single SnO_2, $BiVO_4$, and CuO NPs and the ternary SBC system in PZP removal were also studied. The UV-Vis spectra of the PZP solutions at the end of the processes mentioned above were recorded. The results are shown in **Fig. 4A**. The decrease in the absorption maximum is due to the removed PZP by the various removal methods mentioned above. As shown in the inset, direct photolysis removed only 1.6% PZP molecules during 60 min. On the other hand, the PZP molecules have considerable stability against the arrived photons. On the other hand, no bonds in PZP have broken and no radicals formed during the irradiation process. Further, the surface adsorption has also shown a negligible effect in the PZP removal, and it only removed less than 8% of PZP molecules.

The effects of the heterogeneous photocatalysis in PZP removal were more intense than the direct photolysis and surface adsorption. As shown in the inset, about 11, 15, and 17% of PZP molecules were removed by the CuO, SnO_2, and $BiVO_4$ NPs, respectively. The ternary SBC catalyst showed relatively boosted effects in the PZP removal at the same applied conditions and removed about 24% PZP molecules. In the SBC catalyst used, the moles of the constituent components were the same.

After showing the boosted photocatalytic activity of the SBC system, we studied the effects of the change in the mole ratio of the semiconductors in the ternary SBC system in the PZP removal. The results are shown in **Fig. 4B**. All C/Co values were averaged based on 3 replicates. The small error bars (or standard deviations) were obtained, showing that the difference between the results is not significant. The change in the moles of the semiconductors in the SBC system relatively changed the PZP removal. As shown, when the moles of $BiVO_4$ are two times greater than the others, the lowest C/Co value was achieved, and about 43% of PZP were removed by this catalyst. Thus, this catalyst was used for the subsequent experiments.

Here, the boosted effect of the ternary catalyst and the effects of the change in the mole ratio are illustrated using the Schematic energy diagram in **Fig. 4C**. Under the irradiation process, each of the semiconductors was excited, and the e^-/h^+ pairs were produced in each component. The potential positions of the CB levels are sequenced as CB-$BiVO_4$> CB-CuO> CB-SnO_2. Thus, the migration direction of the photoexcited electrons agrees with this trend, and they can accumulate in the CB-SnO_2 position because this position has the most positive potential position with respect to other CB levels. The conformity of potential positions of VB levels results in the accumulation of the photoinduced holes in the VB-CuO. Thus, these charge carriers'

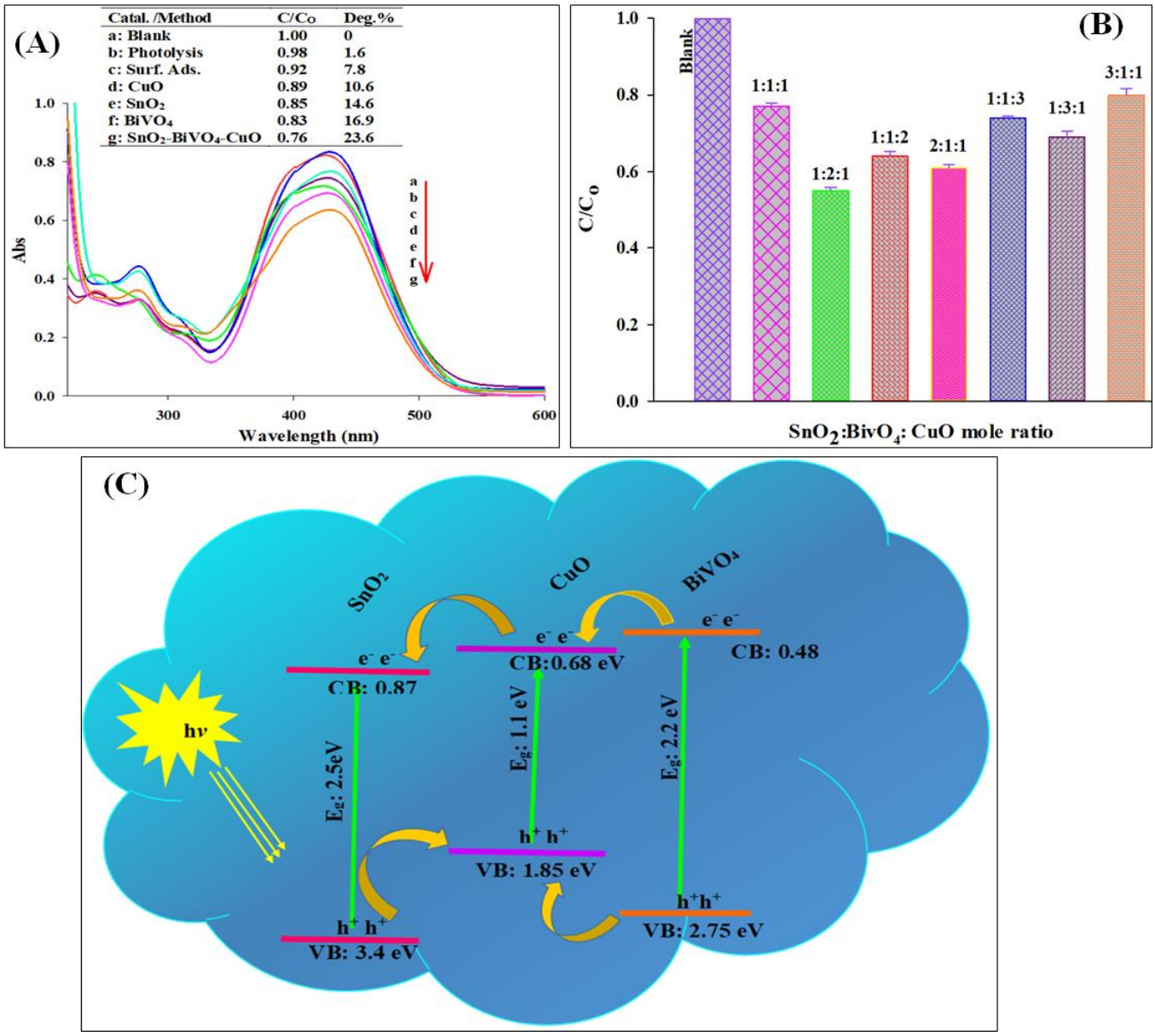

Fig. 4. A) Decrease in UV-Vis absorption spectra of PZP solution during its photodegradation by various removal processes (catalyst dose: 0.5 g L^{-1}, C: 10 ppm, pH: 10, time: 60 min, SnO_2:$BiVO_4$:CuO mole ratio of 1:1:1); **B)** The effect of the change in the SnO_2:$BiVO_4$:CuO mole ratio in the photodegradation extent of PZP by the SnO_2-$BiVO_4$-CuO (conditions as the same of case A, the values were averaged based on triplicate measurements); **C)** Schematic diagram for showing the charge carriers' separation in the ternary SnO_2-$BiVO_4$-CuO coupled system.

transfer can effectively decrease the e^-/h^+ recombination in the proposed ternary catalyst and boost the photocatalytic effect for this catalyst.

According to this discussion, it would be expected that the change in the moles of the constituent semiconductors in the ternary catalyst would result in a change in the photocatalytic activity. The results prove that each component's expected moles would be available to reach the highest charge separation rate. As shown in **Fig. 4B**, when the moles of $BiVO_4$ in the SBC system are two times greater than the others, the best match between the amounts of semiconductors was provided, and the best charge separation was performed.

3.2.2. The kinetic aspects of the process

Generally, the absorbed light at a specific wavelength (A_λ) by a solution can be quantitatively stated by **Eq. (4)** in which I_o and I mean the intensity of the incident light and the transmitted light, respectively.

$$A_\lambda = I_o - I \qquad \textbf{(4)}$$

If the Beers-Lambert law to be met in the applied conditions, the transmitted light can be calculated by

Eq. (5), in which ε is the molar absorptivity, b is the path length, and C is the concentration of the reactant.

$$I = I_o \exp(-\varepsilon bC) \quad \textbf{(5)}$$

Based on Grotthus-Draper's law, the photodegradation rate of a typical photodegradation process depends on the amount of the absorbed photons. Under a constant irradiance, the rate at the time't' can be estimated by the following **Eq. (6)** (k_o is a constant).

$$-dC/dt = k_o.I_o.(1-\exp(-\varepsilon bC)) \quad \textbf{(6)}$$

Over a broad wavelength range and the polychromatic radiation, **Eq. (6)** can be changed to **Eq. (7)**.

$$-dC/dt = \sum k_o.I_o.(1-\exp(-\varepsilon bC)) \quad \textbf{(7)}$$

In the photodegradation process with no absorption by the degradation products, in which k_1 and ε_2 are the rate constant and the reactants' absorption coefficient, the following **Eq. (8)** is applicable.

$$-dC/dt = k_1 (1-\exp(\varepsilon_2 C)) \quad \textbf{(8)}$$

When the degradation products can absorb the arrived photons, proceeding with the photodegradation process causes a decrease in the number of absorbed photons by the reactants. In this condition, the amount of absorbed light by the solution is often more significant than that of the reactant. Thus, **Eq. (8)** can be changed to **Eq. (9)**, in which ε_3 is the absorption coefficient of the degradation products.

$$-dC/dt = k_1 [1-\exp(-(\varepsilon_2 C+ \varepsilon_3(C_o-C)))] (\varepsilon_2 C)/[(\varepsilon_2 C)+ \varepsilon_3(C_o-C)] \quad \textbf{(9)}$$

In a photodegradation process that involves the same spectra (and same molar absorptivity) for the reactant and photodegradation products (or almost same spectra), **Eq. (9)** can be corrected to **Eq. (10)**, because $\varepsilon_2 = \varepsilon_3$. In this equation k is the pseudo-rate constant.

$$-dC/dt = k_1 [1-\exp(-\varepsilon_2 C_o)] [(C)/(C_o] = kC \quad \textbf{(10)}$$

Finally, in the fourth type of the photodegradation process, the concentration of reactant is high, and the value of the exponential term ($\exp(-(\varepsilon_2 C+\varepsilon_3 (Co-C)))$ reaches zero. Thus the rate of the photodegradation process can be studied by the following **Eq. (11)**, which is true for a zero-order rate process.

$$-dC/dt = k_1 \quad \textbf{(11)}$$

Integration of **Eq. (10)** gives the following equation, which is famous as the Hinshelwood equation for a pseudo-first-order reaction kinetics [76-85].

$$\ln(C/Co) = -kt \quad (\text{or } C_t = C_o e^{-kt}) \quad \textbf{(12)}$$

Commonly, the heterogeneous photodegradation processes have conditions in which both the reactants and the degradation products can absorb arrived photons. Thus, the kinetics of the process obeys the pseudo-first-order kinetics. To study the kinetics of the process, photodegradation experiments were done in various irradiation times. The results are shown in **Fig. 5A**, in which the decrease in the C/Co value during the time confirms that more PZP molecules have degraded during the time. The inset of the figure shows a typical Hinshelwood plot for the process, in which the slope shows the pseudo-first-order rate constant for the process. The k-value of 9.9×10^{-3} min^{-1} corresponds to the $t_{1/2}$-value of 70 min according to the 0.693/k formula.

In the next step, the photodegraded PZP solutions were subject to the chemical oxygen demand (COD) experiment. Generally, COD measures the required oxygen to mineralize the organic pollutants present in an aqueous medium. Thus, a lower COD value means lower pollution for the tested sample. As shown in **Fig. 5B**, the remaining COD for the PZP solutions during the photodegradation process was decreased. This confirms that the PZP degradation products were mineralized during the photodegradation process, and the pollution of the solution was decreased. On the other hand, the degradation products of PZP solutions were mineralized to CO_2, H_2O, etc., during the process. Based on the results obtained in the COD experiments, the Hinshelwood plot was constructed and is shown in the inset of **Fig. 5B**. The linear plot showed a slope of 0.01 min^{-1} which corresponds to the $t_{1/2}$-value of 69.3 min. The results are very close to the values obtained based on the photodegradation experiments. On the other hand, the photodegradation products produced during the process can rapidly mineralize into inorganic species. Thus, the proposed catalyst can be served as an effective catalyst for mineralizing PZP molecules in wastewater samples.

3.2.3. Reusing results

Some photodegradation experiments were carried out in various irradiation times for evaluating the catalyst for use in successive runs and its stability. After each experiment, the catalyst was separated by centrifugation and dried at 100 ºC for 5 min and used in the next run. The obtained results are shown in **Fig. 6**. As shown in **Fig. 6B**, the rate constants of 0.012, 0.011, and 0.010 min^{-1} were obtained for the first to third run. Comparing the k-values confirms rate constant are close, and no significant decrease in the activity of the ternary catalyst was achieved after three successive using runs.

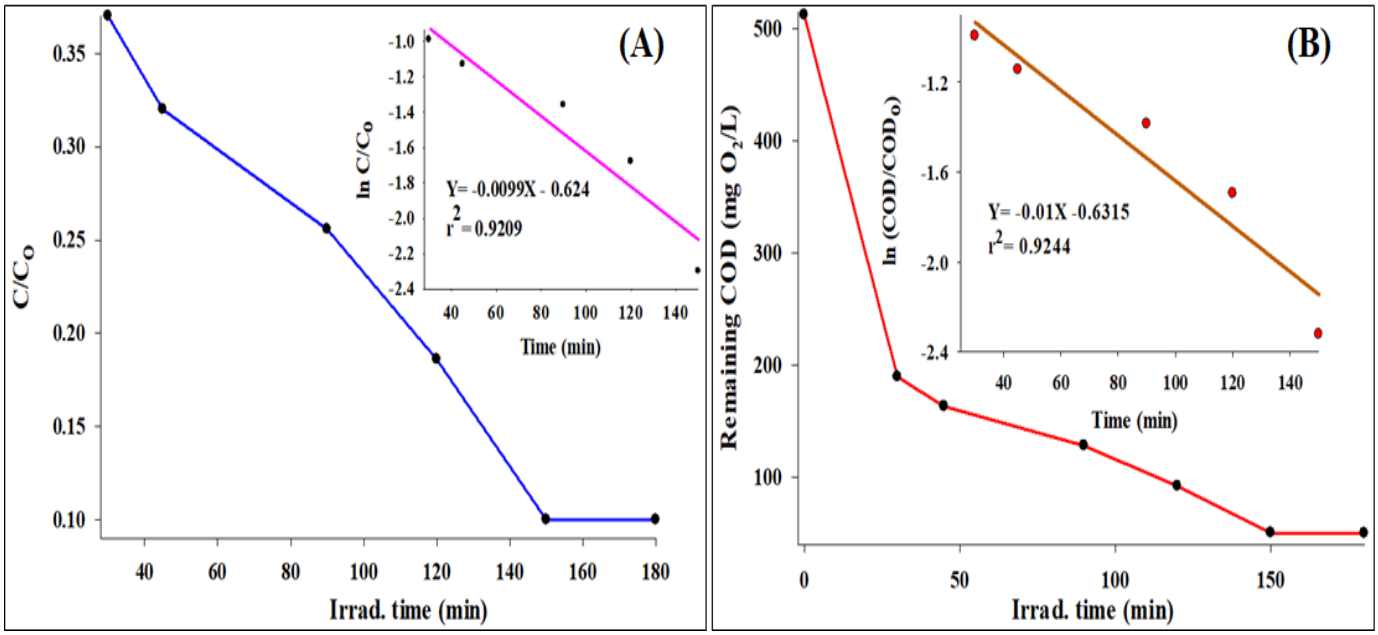

Fig. 5. A) Effect of irradiation time on PZP degradation, (Inset: plot of ln(C/Co) vs time for calculation of the rate constant (pH: 5, C_{PhP}: 3.35 ppm, dosage: 0.55 g L^{-1}); **B)** Change in COD of PZP solutions during the photodegradation process done in the resulting photodegraded solution in case A (Inset: Typical Hinshelwood plotconstructed based on the COD results).

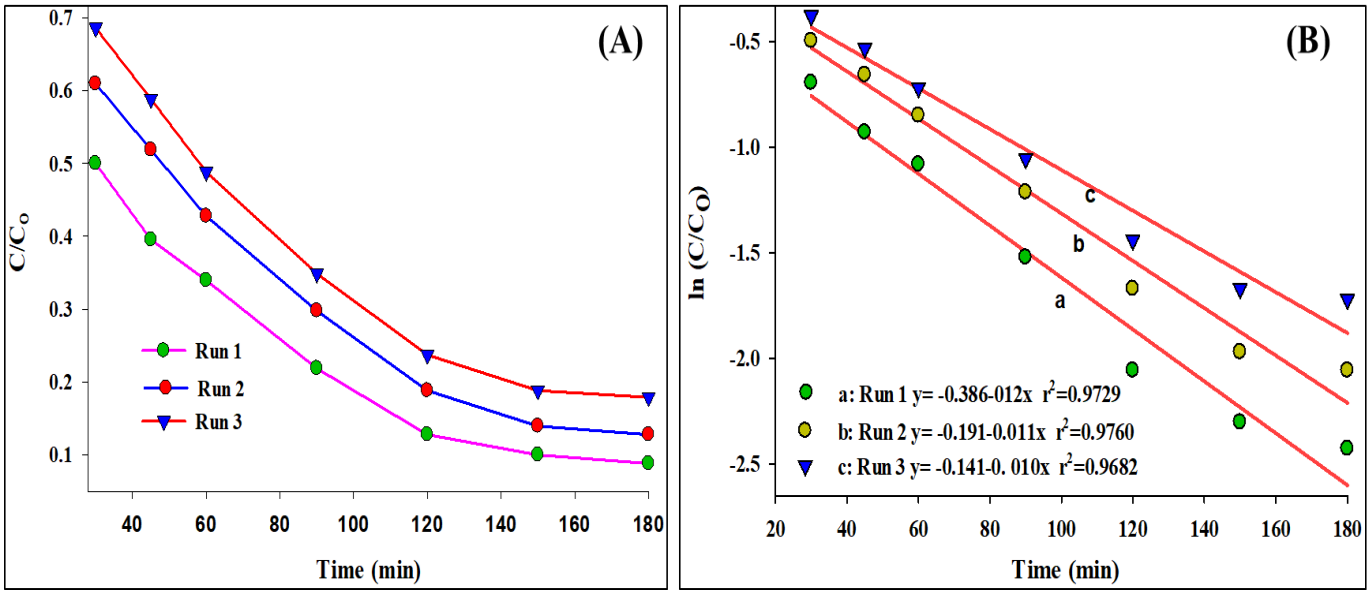

Fig. 6. Reusability of the $SnO_2/BiVO_4/CuO$ photocatalyst in photodegradation of PZP (pH: 5, C_{PZP}: 3.35 ppm, catalyst dosage: 0.55 g/L).

4. Conclusions

A boosted enhanced photocatalytic activity in the PZP photodegradation was obtained when the SnO_2, $BiVO_4$, and CuO nanoparticles (NPs) were coupled (SBC catalyst). This is due to a better charge separation between the coupled semiconductors, which resulted in matching their potential positions of the VB and CB positions. Besides, the charge separation extent in the SBC sample depends on the amounts of the semiconductors involved. On the other hand, further to the suitable potential position, the balance between the mass of the semiconductors is also essential in the charge separation extent. Accordingly, when the moles of $BiVO_4$ are twice greater than the others, the highest photodegradation efficiency was obtained. The slopes of the Hinshelwood plots for both photodegradation and the COD processes were close, confirming that the photodegradation intermediates can rapidly mineralize into carbon dioxide, water, and other inorganic species during the PZP photodegradation process.

References

[1] Liuwei Wang, Deyi Hou, Yining Cao, Yong Sik Ok, Filip M.G. Tack, Jörg Rinklebe, David O'Connor, Remediation of mercury contaminated soil, water, and air: A review of emerging materials and innovative technologies, Environ. Inter. 134 (2020) 105281.

[2] Yang Wu, Chung-Yu Guan, Nicholas Griswold, Li-yuan Hou, Xin Fang, Anyi Hu, Zhi-qiang Hu, Chang-Ping Yu, Zero-valent iron-based technologies for removal of heavy metal(loid)s and organic pollutants from the aquatic environment: Recent advances and perspectives, J. Cleaner Production, 277 (2020) 123478.

[3] Sh. Ahmad Bhat, F. Zafar, A. Hossain Mondal, Abdul Kareem, A. Ullah Mirza, Sh. Khan, A. Mohammad, Qazi Mohd. Rizwanul Haq, N. Nishat, Photocatalytic degradation of carcinogenic Congo red dye in aqueous solution, antioxidant activity and bactericidal effect of NiO nanoparticles, J. Iran. Chem. Soc. 17 (2020) 215–227.

[4] I. R. Segundo, E. Freitas, S. Landi Jr., Manuel F. M. Costa, Joaquim O. Carneiro, Smart, Photocatalytic and Self-Cleaning Asphalt Mixtures: A Literature Review, Coatings 9 (2019) 696 (1-22 pages) doi:10.3390/coatings9110696.

[5] P. Raizada, A. Sudhaik, P. Singh, P. Shandilya, Vinod Kumar Gupta, A. Hosseini-Bandegharaei, Shilpi Agrawal, Ag_3PO_4 modified phosphorus and sulphur co-doped graphitic carbon nitride as a direct Z-scheme photocatalyst for 2, 4-dimethyl phenol degradation, J. Photochem. Photobiol. A: Chem. 374 (2019) 22–35.

[6] H. Karimi-Maleh, M. Shafieizadeh, M. A. Taher, F. Opoku, E. Muriithi Kiarii, P. P. Govender, S. Ranjbari, M. Rezapour, Y. Orooji, The role of magnetite/graphene oxide nano-composite as a high-efficiency adsorbent for removal of phenazopyridine residues from water samples, an experimental/theoretical investigation, J. Mol. Liq. 298 (2020) 112040.

[7] Abhinandan Kumar, P. Raizada, A. Hosseini-Bandegharaei, Vijay Kumar Thakur, Van-Huy Nguyen, P. Singh, C-, N-Vacancy defect engineered polymeric carbon nitride towards photocatalysis: viewpoints and challenges, J. Mater. Chem. A 9 (2021) 111-153.

[8] H. Karimi-Maleh, B. Ganesh Kumar, S. Rajendran, J. Qin, S. Vadivel, D. Durgalakshmi, F. Gracia, M. Soto-Moscoso, Y. Orooji, F. Karimi, Tuning of metal oxides photocatalytic performance using Ag nanoparticles integration, J. Mol. Liq. 314 (2020) 113588.

[9] A. Kumar, P. Raizada, P. Singh, R. V Saini, A. K Saini, A. Hosseini-Bandegharaei, Perspective and status of polymeric graphitic carbon nitride based Z-scheme photocatalytic systems for sustainable photocatalytic water purification, Chem. Eng. J. 391 (2020) 123496.

[10] H. Karimi-Maleh, A. Ayati, S. Ghanbari, Y. Orooji, B. Tanhaei, F. Karimi, M. Alizadeh, J. Rouhi, L. Fu, M. Sillanpää, Recent advances in removal techniques of Cr(VI) toxic ion from aqueous solution: A comprehensive review, J. Mol. Liq. 329 (2021) 115062.

[11] H. Karimi-Maleh, S. Ranjbari, B. Tanhaei, A. Ayati, Y. Orooji, M. Alizadeh, F. Karimi, S. Salmanpour, J. Rouhi, M. Sillanpää, F. Sen, Novel 1-butyl-3-methylimidazolium bromide impregnated chitosan hydrogel beads nanostructure as an efficient nanobio-adsorbent for cationic dye removal: Kinetic study, Environ. Res. 195 (2021) 110809.

[12] H. Karimi-Maleh, M. Lütfi Yola, N. Atar, Y. Orooji, F. Karimi, P. Senthil Kumar, J. Rouhi, M. Baghayeri, A novel detection method for organophosphorus insecticide fenamiphos: Molecularly imprinted electrochemical sensor based on core-shell Co_3O_4@MOF-74 nanocomposite, J. Colloid Interf. Sci. 592 (2021) 174–185.

[13] H. Karimi-Maleh, M. Alizadeh, Y. Orooji, F. Karimi, M. Baghayeri, J. Rouhi, S. Tajik, H. Beitollahi, S. Agarwal, V.K. Gupta, S. Rajendran, S. Rostamnia, L. Fu, F. Saberi-Movahed, S. Malekmohammadi, Guanine-Based DNA Biosensor Amplified with Pt/SWCNTs Nanocomposite as Analytical Tool for Nanomolar Determination of Daunorubicin as an Anticancer Drug: A Docking/Experimental Investigation, Ind. Eng. Chem. Res. 60 (2021) 816-823.

[14] Sh. Ahmad Bhat, F. Zafar, A. Hossain Mondal, Abdul Kareem, A. Ullah Mirza, Sh. Khan, A. Mohammad, Qazi Mohd. Rizwanul Haq, N. Nishat, Photocatalytic degradation of carcinogenic Congo red dye in aqueous solution, antioxidant activity and bactericidal effect of NiO nanoparticles, J. Iran. Chem. Soc. 17 (2020) 215–227

[15] Dongfang Zhang, Jiaxun Wang, Visible-light-responsive bismuth oxybromide/graphite-like C_3N_4 hybrid material and its application in photocatalysis via internal electric field, J. Iran. Chem. Soc. 16 (2019) 827-839.

[16] N. Pourshirband, A. Nezamzadeh-Ejhieh, Seyed Nezamoddin Mirsattari, The coupled AgI/BiOI catalyst: Synthesis, brief characterization, and study of the kinetic of the EBT photodegradation, Chem. Phys. Lett. 761 (2020) 138090.

[17] A. Pourtaheri, A. Nezamzadeh-Ejhieh, Enhancement in photocatalytic activity of NiO by supporting onto an Iranian clinoptilolite nano-particles of aqueous solution of cefuroxime pharmaceutical capsule, Spectrochim. Acta Part A: Molec. Biomolec. Spect. 137 (2015) 338–344.

[18] S.P. Meshram, P.V. Adhyapak, U.P. Mulik, D.P. Amalnerkar, Facile synthesis of CuO nanomorphs and their morphology dependent sunlight driven photocatalytic properties, Chem. Eng. J. 204–206 (2012) 158–168.

[19] M. Karimi Shamsabadi, M. Behpour, Fabricated CuO–ZnO/nanozeolite X heterostructure with enhanced photocatalytic performance: mechanism investigation and degradation pathway, Mater. Sci. Eng. B 269 (2021) 115170.

[20] P. Eghbali, A. Hassani, B. Sündü, Ö. Metin, Strontium titanate nanocubes assembled on mesoporous graphitic carbon nitride ($SrTiO_3$/mpg-C_3N_4): Preparation, characterization and catalytic performance. J. Mol. Liq. 290 (2019) 111208.

[21] A. Hassani, P. Eghbali, Ö. Metin, Sonocatalytic removal of methylene blue from water solution by cobalt ferrite/mesoporous graphitic carbon nitride ($CoFe_2O_4$/mpg-C_3N_4) nanocomposites: response surface methodology approach, Environ. Sci. Poll. Res. 25 (2018) 32140-32155.

[22] R. Kumar, A. Sudhaik, P. Raizada, A. Hosseini-Bandegharaei, Vijay Kumar Thakurd, A. Saini, V. Saini, P. Singh, An overview on bismuth molybdate based

photocatalytic systems: Controlled morphology and enhancement strategies for photocatalytic water purification, J. Environ. Chem. Eng. 8 (2020) 104291.
[23] Sudhaik, Anita, Pankaj Raizada, Saloni Thakur, Reena V. Saini, Adesh K. Saini, Pardeep Singh, Vijay Kumar Thakur, Van-Huy Nguyen, Aftab Aslam Parwaz Khan, and Abdullah M. Asiri, Synergistic photocatalytic mitigation of imidacloprid pesticide and antibacterial activity using carbon nanotube decorated phosphorus doped graphitic carbon nitride photocatalyst, J. Taiwan Institute Chem. Eng. 113 (2020) 142-154.
[24] Kumar, Abhinandan, P. Raizada, P. Singh, A. Hosseini-Bandegharaei, Vijay K. Thakur, Facile synthesis and extended visible light activity of oxygen and sulphur co-doped carbon nitride quantum dots modified Bi2MoO6 for phenol degradation, J. Photochem. Photobiol. A: Chem. 397 (2020) 112588.
[25] S. Dharmraj Khairnar, M. Rajendra Patil, V. Shankar Shrivastava, Hydrothermally synthesized nanocrystalline Nb_2O_5 and its visible-light photocatalytic activity for the degradation of congo red and methylene blue, Iran. J. Catal. 8(2) (2018) 143-150.
[26] A. Hassani, M. Faraji, P. Eghbali, Facile fabrication of mpg-C_3N_4/Ag/ZnO nanowires/Zn photocatalyst plates for photodegradation of dye pollutant, J. Photochem. Photobiol. A: Chem. 400 (2020) 112665.
[27] A. Omidi, A. Habibi-Yangjeh, Microwave-assisted method for preparation of Sb-doped ZnO nanostructures and their photocatalytic activity, J. Iran. Chem. Soc. 11 (2014) 457–465.
[28] P. Raizada, Aftab Aslam Parwaz Khan, P. Singh, Construction of carbon nanotube mediated Fe doped graphitic carbon nitride and Ag_3VO_4 based Z-scheme heterojunction for H_2O_2 assisted 2, 4 dimethyl phenol photodegradation, Sep. Pur. Techn. 247 (2020) 116957.
[29] M. Bordbar, S. Jafari, A. Yeganeh-Faal, B. Khodadadi, Influence of different precursors and Mn doping concentrations on the structural, optical properties and photocatalytic activity of single-crystal manganese-doped ZnO, J. Iran. Chem. Soc. 14 (2017) 897–906.
[30] P. Shilpa, P. Raizada, V. Hasija, P. Singh, V. K. Thakur, Van-Huy Nguyen, Recent advances in photocatalytic multivariate metal organic framework (MOFs) based nanostructures toward renewable energy and the removal of environmental pollutants, Mater. Today Energy 19 (2020) 100589.
[31] M. Zebardast, A. Fallah Shojaei, Kh. Tabatabaeian, Enhanced removal of methylene blue dye by bimetallic nano-sized MOF-5s, Iran. J. Catal. 8(4) (2018) 297-309
[32] A Bagheri-Ghomi, V. Ashayeri, Photocatalytic efficiency of $CuFe_2O_4$ by supporting on clinoptilolite in the decolorization of acid red 206 aqueous solutions, Iran. J. Catal. 2(3) (2012) 135-140
[33] H. Derikvandi, A. Nezamzadeh-Ejhieh, Increased photocatalytic activity of NiO and ZnO in photodegradation of a model drug aqueous solution: Effect of coupling, supporting, particles size and calcination temperature, J. Hazard. Mater. 321 (2017) 629–638
[34] S. Dianat, Visible light induced photocatalytic degradation of direct red 23 and direct brown 166 by $InVO_4$-TiO_2 nanocomposite, Iran. J. Catal. 8(2) (2018) 121-132.
[35] K. Anil Isai, Vinod Shankar Shrivastava, Photocatalytic degradation of methyl orange using ZnO and Fe doped ZnO: A comparative study, Iran. J. Catal. 9(3) (2019) 259-268
[36] M.L. Maya-Treviño, J.L. Guzmán-Mar, L. Hinojosa-Reyes, A. Hernández-Ramírez, Synthesis and photocatalytic activity of ZnO-CuPc for methylene blue and potassium cyanide degradation, Mater. Sci. Semicond. Proc. 77 (2018) 74-82.
[37] A. Hassani, P. Eghbali, Ö. Metin, Sonocatalytic removal of methylene blue from water solution by cobalt ferrite/mesoporous graphitic carbon nitride ($CoFe_2O_4$/mpg-C_3N_4) nanocomposites: response surface methodology approach, Environ. Sci. Poll. Res. 25 (2018) 32140-32155.
[38] Hassani, P. Eghbali, B. Kakavandi, K.-Y. A. Lin, F. Ghanbari. Acetaminophen removal from aqueous solutions through peroxymonosulfate activation by $CoFe_2O_4$/mpg-C_3N_4 nanocomposite: Insight into the performance and degradation kinetics. Environ. Techn. & Innovation, 20 (2020) 101127.
[39] A. Buthiyappan, Abdul R. Abdul Aziz, Wan Mohd Ashri Wan Daud, Recent advances and prospects of catalytic advanced oxidation process in treating textile effluents, Rev. Chem. Eng. 32(1) (2015) 1-47
[40] Shirin Ghattavi, A. Nezamzadeh-Ejhieh, A visible light driven AgBr/g-C_3N_4 photocatalyst composite in methyl orange photodegradation: Focus on photoluminescence, mole ratio, synthesis method of g-C_3N_4 and scavengers, Composites Part B 183 (2020) 107712.
[41] Quanlong Xu, Liuyang Zhang, Jiaguo Yu, Swelm Wageh, Ahmed A. Al-Ghamdi, Mietek Jaroniec, Direct Z-scheme photocatalysts: Principles, synthesis and applications, Mater. Today 21 (2018) 1042-1063.
[42] Aftab Aslam Parwaz Khan, P. Singh, P. Raizada, Abdullah M. Asiri, Synthesis of magnetically separable $Bi_2O_2CO_3$/carbon nanotube/$ZnFe_2O_4$ as Z-scheme heterojunction with enhanced photocatalytic activity for water purification, J. Sol-Gel Sci. Technol. 95(2) (2020) 408-422.
[43] N. Omrani, A. Nezamzadeh-Ejhieh, Focus on scavengers' effects and GC-MASS analysis of photodegradation intermediates of sulfasalazine by Cu_2O/CdS nanocomposite, Sep. Purification Technol. 235 (2020) 116228.
[44] S. Patial, P. Raizada, V. Hasija, P. Singh, V. Kumar Thakur, V.-H. Nguyen, Recent advances in photocatalytic multivariate metal organic frameworks-based nanostructures toward renewable energy and the removal of environmental pollutants, Mater. Today Energy 19 (2021) 100589.
[45] P. Singh, P. Shandilya, P. Raizada, A. Sudhaik, A. Rahmani-Sani, A. Hosseini-Bandegharaei, Review on various strategies for enhancing photocatalytic activity of graphene based nanocomposites for water purification, Arabian J. Chem. (2020) 13, 3498–3520.
[46] Sonu, V. Dutta, Sheetal Sharma, P. Raizada, A. Hosseini-Bandegharaei, V. K. Gupta, P. Singh, Review on augmentation in photocatalytic activity of CoFe2O4 via

heterojunction formation for photocatalysis of organic pollutants in water, J. Saudi Chem.Soc. 23 (2019) 1119–1136.
[47] Yunfang Huang, Hui Xu, Dan Luo, Qiyao Guo, Yuezhu Zhao, Yu Fang, Yuelin Wei, Leqing Fan, Jihuai Wu, Visible light-driven flower-like Bi/$BiOCl_xBr_{(1-x)}$ heterojunction with excellent photocatalytic performance, J. Iran. Chem. Soc. 16 (2019) 2743–2754.
[48] H. Derikvandi, M. Vosough, A. Nezamzadeh-Ejhieh, A comprehensive study on the enhanced photocatlytic activity of a double-shell mesoporous plasmonic Cu@Cu_2O/SiO_2 as a visible-light driven nanophotocatalyst, Environ. Sci. Pollution Res. 27 (2020) 27582–27597.
[49] N. Jalili-Jahani, B. Hemmateenejad, M. Shamsipur, Gold-decorated Fe_3O_4 nanoparticles for efficient photocatalytic degradation of ampicillin: a chemometrics investigation, J. Iran. Chem. Soc. 17 (2020) 1173–1182.
[50] H. Derikvandi, M. Vosough, A. Nezamzadeh-Ejhieh, A novel double Ag@AgCl/Cu@Cu_2O plasmonic nanostructure: Experimental design and LC-Mass detection of tetracycline degradation intermediates, Inter. J. Hydrogen Energy 46 (2021) 2049 -2064.
[51] K. Zhou, R. Wang, B. Xu, Y. Li, Synthesis, characterization and catalytic properties of CuO nanocrystals with various shapes, Nanotechnology 17 (2006) 3939-3943.
[52] K. Prashant B, K. Kailas H, Green synthesis and characterization of SnO_2 and ZnO nanoparticles: study their electrical conductivity and gas sensing properties, der Chemic**.** Sinica. 7 (2016) 29-35.
[53] S. Selvarajan, A. Suganthi, M. Rajarajan, K. Arunprasath, Highly efficient $BiVO_4/WO_3$ nanocomposite towards superior photocatalytic performance, Powder Technol. 307 (2017) 203-212.
[54] S. Mortazavi, H. Aghaei, Make proper surfaces for immobilization of enzymes: Immobilization of lipase and α-amylase on modified Na-sepiolite, Int. J. Biol. Macromol. 164 (2020) 1-12.
[55] A. R. Massah, R. Javad Kalbasi, S. Kaviyani, Synthesis, characterization, and application of a manganese Schiff base complex containing heterogeneous hybrid catalyst, RSC Adv. 3 (2013) 12816-12825.
[56] A. Bhagwat, S. Sawant, B. Ankamwar, C. Mahajan, Synthesis of nanostructured tin oxide (SnO_2) powders and thin films by sol-gel method, J. Nano- Electron. Phys. 7 (2015) 04037.
[57] G. Patil1, D. Kajale, V. Gaikwad1, G. Jain, Preparation and characterization of SnO_2 nanoparticles by hydrothermal route, Int. Nano Lett. 2 (2012) 1-5.
[58] H. E. A. Mohamed, B. T. Sone, X. G. Fuku, M. S. Dhlamini, M. Maaza, Green synthesis of $BiVO_4$ nanorods via aqueous extracts of callistemon viminalis, AIP Conference Proceedings 1962, 040004 (2018); doi: 10.1063/1.5035542.
[59] P. Brack, Jagdeep S. Sagu, T. A. Nirmal Peiris, Andrew McInnes, Mauro Senili, K. G. Upul Wijayantha, Frank Marken, Elena Selli, Aerosol-Assisted CVD of Bismuth Vanadate Thin Films and Their Photoelectrochemical Properties, Chem. Vap. Deposition 20 (2014) 1–5.
[60] R. Etefagh, E. Azhir, N. Shahtahmasebi, Synthesis of CuO nanoparticles and fabrication of nanostructural layer biosensors for detecting Aspergillusniger fungi, Scientia Iranica, 20 (2013) 1055-1058.
[61] V. Vellora, Thekkae Padil, M. Černík, Green synthesis of copper oxide nanoparticles using gum karaya as a biotemplate and their antibacterial application, Inter. J. Nanomedicine 8 (2013) 889–898.
[62] Sharma Kirti, P. Raizada, A. Hosseini-Bandegharaei, P. Thakur, R. Kumar, V. K. Thakur, Van-Huy Nguyen, P. Singh, Fabrication of efficient CuO/graphitic carbon nitride based heterogeneous photo-Fenton like catalyst for degradation of 2, 4 dimethyl phenol, Process Safety Environ. Protec. 142 (2020) 63-75.
[63] Solmaz Aghdasi, Mohammad Shokri, Photocatalytic degradation of ciprofloxacin in the presence of synthesized ZnO nanocatalyst: The effect of operational parameters, Iran. J. Catal. 6(5) (2016) 481-487.
[64] P. Scherrer, Bestimmung der Größe und der inneren Struktur von Kolloidteilchen mittels Röntgenstrahlen, Göttinger Nachrichten Gesell. 2 (1918) 98-100.
[65] A. Patterson, *The Scherrer Formula for X-Ray Particle Size Determination, Phys. Rev. 56(10) (1939) 978–982.*
[66] Shokufeh Aghabeygi, R. Kia Kojoori, H. Vakili Azad, Sonosynthesis, characterization and photocatalytic degradation property of nanoZnO/zeoliteA, Iran. J. Catal. 6(3) (2016) 275-279.
[67] U. Holzwarth, N. Gibson, The Scherrer equation versus the 'Debye-Scherrer equation', Nature Nanotech 6 (2011) 534.
[68] F. T. Leitão Muniz, M. A. Ribeiro Miranda, C. Morilla dos Santos, J. Marcos Sasaki, The Scherrer equation and the dynamical theory of X- ray diffraction, Cta Crystal. Section A: Fund. Adv. 72 (2016) 385-390.
[69] N. Lotfian, AmirAbbas Nourbakhsh, Seyed Nezamoddin Mirsattari, A. Saberi, Kenneth J.D. Mackenzie, A comparison of the effect of nanostructured $MgCr_2O_4$ and $FeCr_2O_4$ additions on the microstructure and mechanical properties of direct-bonded magnesia-chrome refractories, Ceramics Inter. 46 (2020) 747-754.
[70] N. Jeevanantham, O. N. Balasundaram, High-performance visible light photocatalytic activity of cobalt (Co) doped CdS nanoparticles by wet chemical route, J. Iran. Chem. Soc. 16 (2019) 243–251.
[71] M. Bordbar, Z. Sayban, A. Yeganeh-Faal, B. Khodadadi, Incorporation of Pb^{2+}, Fe^{2+} and Cd^{2+} ions in ZnO nanocatalyst for photocatalytic activity, Iran. J. Catal. 8(2) (2018) 113-120.
[72] V. Taghvaei, A. Habibi-Yangjeh, M. Behboudnia, Simple and low temperature preparation and characterization of CdS nanoparticles as a highly efficient photocatalyst in presence of a low-cost ionic liquid, J. Iran. Chem. Soc. 7 (2010) S175–S186.
[73] R. Javad Kalbasi, A. R. Massah, F. Zamani, Alex D. Bain, Bob Berno, Metal (Co, Mn)-amine-functionalized mesoporous silica SBA-15:synthesis, characterization and catalytic properties in hydroxylation of benzene, J. Porous Mater. 18 (2011) 475–482.
[74] M. Khozeymeh Nezhad, H. Aghaei, Tosylated cloisite as a new heterofunctional carrier for covalent immobilization of lipase and its utilization for production of biodiesel from waste frying oil, Renew. Energy 164 (2021) 876-888.

[75] R. Javad Kalbasi, A. R. Massah, B. Daneshvarnejad, Preparation and characterization of bentonite/PS-SO_3H nanocomposites as an efficient acid catalyst for the Biginelli reaction, Appl. Clay Sci. 55 (2012) 1–9.
[76] I. Matsuura, M. Imaizumi, M. Su Giyama, Method of kinetic analysis of photodegradation: Nifedipine in solutions, Chem. Pharm. Bull. 38 (1990) 1692-1696.
[77] M. Balakrishnan, R. John, Properties of sol-gel synthesized multiphase TiO2 (AB)-ZnO (ZW) semiconductor nanostructure: An effective catalyst for methylene blue dye degradation, Iran. J. Catal. 10(1) (2020) 1-16.
[78] N. Assi, M. S. Tehrani, P. Aberoomand Azar, Syed Waqif Husain, Microwave-assisted sol–gel synthesis of $Fe_{2.9}O_4$/ZnO core/shell nanoparticles using ethylene glycol and its use in photocatalytic degradation of 2-nitrophenol, J. Iran. Chem. Soc. 14 (2017) 221–232.
[79] N. Pourshirband, A. Nezamzadeh-Ejhieh, An efficient Z-scheme CdS/g-C_3N_4 nano catalyst in methyl orange photodegradation: Focus on the scavenging agent and mechanism, J. Mol. Liq. 335 (2021) 116543.
[80] V. Mirkhani, S. Tangestaninejad, M. Moghadam, M. H. Habibi, A. Rostami Vartooni, Photodegradation of aromatic amines by Ag-TiO_2 photocatalyst, J. Iran. Chem. Soc. 6 (2009) 800–807.
[81] A. Mahmood, Xiao Wang, Xiaofeng Xie, Jing Sun, Degradation behavior of mixed and isolated aromatic ring containing VOCs: Langmuir-*Hinshelwood* kinetics, *photodegradation*, in-situ FTIR and DFT studies, J. Environ. Chem. Eng. 9 (2021) 105069.
[82] M. Falamarzi, E. Akbarzadeh, M. R. Gholami, Zeolitic imidazolate framework-derived Ag/C/ZnO for rapid reduction of organic pollutant, J. Iran. Chem. Soc. 16 (2019) 1105–1111.
[83] P. Raizada, J. Kumari, P. Shandilya, P. Singh, Kinetics of photocatalytic mineralization of oxytetracycline and ampicillin using activated carbon supported ZnO/$ZnWO_4$ nanocomposite in simulated wastewater, Desal. Water Treat. 79 (2017) 204–213.
[84] F. Yousefi, A. Nezamzadeh-Ejhieh, Photodegradation of phenazopyridine in an aqueous solution by CdS-WO_3 nanocomposite, Desal. Water Treat. 182 (2020) 299-308.
[85] Shirin Ghattavi, A. Nezamzadeh-Ejhieh, A brief study on the boosted photocatalytic activity of AgI/WO_3/ZnO in the degradation of Methylene Blue under visible light irradiation, Desal. Water Treat. 166 (2019) 92–104.